photonics

MDPI

Article

On-Chip Volume Refractometry and Optical Binding of Nanoplastics Colloids in a Stable Optofluidic Fabry–Pérot Microresonator

Noha Gaber [1,2,*], Frédéric Marty [2], Elodie Richalot [2] and Tarik Bourouina [2]

[1] Center for Nanotechnology and Program of Nanotechnology and Nanoelectronics Engineering, Zewail City of Science and Technology, Giza 12578, Egypt
[2] ESYCOM Lab, UMR 9007 CNRS, Université Gustave Eiffel, 77454 Marne-la-Vallée, France
* Correspondence: ngaber@zewailcity.edu.eg

Abstract

Plastic pollution raises concerns for health and the environment. Plastics are not biodegradable but gradually erode to microplastic and nanoplastic particles spreading almost everywhere. Nanoplastics exhibit colloidal behavior. Thereby, their analysis can be accomplished by refractometry, preferably by an on-chip tool. We present a study of such colloids using a microfabricated Fabry–Pérot cavity with curved mirrors, which holds a capillary microtube used both for fluid handling and light collimation, resulting in an optically stable microresonator. Despite the numerous scatterers within the sample, the sub-millimeter scale cavity provides the advantages of reduced interaction length while maintaining light confinement. This significantly reduces optical loss and hence keeps resonance modes with quality factors (resonant frequency/bandwidth) above 1100. Therefore, small quantities of colloids can be measured by the interference spectral response through the shift in resonant wavelengths. The particles' Brownian motion potentially causing perturbations in the spectra can be overcome either by post-measurement cross-correlation analysis or by avoiding it entirely by taking the measurements at once by a wideband source and a spectrum analyzer. The effective refractive index of solutions with solid contents down to 0.34% could be determined with good agreement with theoretical predictions. Even lower detection capabilities might be attained by slightly altering the technique to cause particle aggregation achieved solely by light.

Keywords: Fabry–Pérot; nanoplastics; on chip measurement; optofluidic device; optical micro-resonators; colloids spectrometry; colloidal refractometry

Check for updates

Received: 30 November 2025
Revised: 4 January 2026
Accepted: 6 January 2026
Published: 20 January 2026

Copyright: © 2026 by the authors. Licensee MDPI, Basel, Switzerland. This article is an open access article distributed under the terms and conditions of the Creative Commons Attribution (CC BY) license.

1. Introduction

Plastic pollution has increasing impact on health and the environment [1,2]. Plastics are neither biodegradable nor soluble in water but gradually wear away until becoming microplastic (MPs, 1 µm–5 mm) or nanoplastic particles (NPs, <1 µm). The latter may pose higher ecological and health risks [3]. These particles can contaminate water and aquatic systems, food and beverages, and even animal and human bodies [4]. Thereby, a simple tool to measure them is of great usefulness.

Several efforts have been made for plastic particle detection, with the majority of attention focused on MPs [5]. Among these efforts, techniques such as near-infrared spectroscopy (NIR) [6], nuclear magnetic resonance (NMR) [7], inductively coupled plasma mass spectrometry (ICP-MS) [8], surface plasmon resonance (SPR) [9], and florescence [10]

have been used. On the other hand, research on NPs with diameters below 1 µm is limited, although such particles can cross biological borders, posing a greater health risk than MPs. Despite the difficulty of imaging such tiny sizes, Ludescher et al. were able to do so using colorometric techniques [11]; Raman microscopy has also proven useful [12]. Apart from imaging that requires bulky microscopes, NPs can have other avenues to be detected, as they exhibit colloidal behavior [5]. It is worth noting that the classification of NPs' maximum size limit is debated in the literature [5]. It is set as 100 nm in some publications, while it is as 1000 nm in others. In this work, we will adopt the latter, as it fits with the colloidal behavior still observed for particles above 100 nm and below 1000 nm in diameter. Colloids characterization—including NPs—can be accomplished optically by infrared spectroscopy [13], ultraviolet–visible (UV-Vis) spectroscopy [14], and ellipsometry [15], or by depending on the phenomena of scattering for some techniques. The method of determining the effective refractive index (ERI) of the colloid has been less widely adopted, probably because of the theoretical and experimental difficulties that faces determining the value of the ERI of turbid media, especially when particle concentrations is high or particle sizes are comparable to the light wavelength, as will be detailed. One of the advantages of this method is that it can be performed mostly without the need to preprocess the colloidal samples [16,17].

The previous colloidal refractometry performed in the literature can be categorized into two major groups: the first one combines those that rely on Fresnel's relations and use the usual Snell's law in calculating the refractive index, including the critical angle [16–20], Brewster angle [21–23], and beam deviation methods [24,25]. These techniques form the vast majority of the experimental attempts to measure the ERI of turbid media found in the literature. Unfortunately, the use of these angle-depending methods in colloidal measurements resulted in some deviation from the expected values from calculations [18,24], and it has been mathematically proved to be unsuitable for turbid medium [26]. More specifically, Snell's law in its basic form is valid only for transparent and homogeneous media, and is not valid when one medium (or both) has complex refractive index [18,27]. In this case, the readings obtained from the measurements give apparent refractive indices different from the true values of the sample. And the error strongly depends on the angle of refraction. For some workers, the error was estimated and considered negligible, provided the turbidity—and hence absorption—remained below certain 'accepted' values [18,24,27]. Some attempts have been made to mitigate the error either empirically [28] or by adjusting the models [29,30]. However, they mostly did not rely on solid scientific validation, and some of them exhibited some doubts [31]. To come out of this debate, methods that do not involve reflection and do not rely on Fresnel's equations are preferable. That leads us to the second group, which comprises the methods relying on the transmitted wave parameter changes, such as the intensity in the scattering modeling [32–34] and phase delay. Light scattering modeling—sometimes called diffuse transmission spectroscopy (DTS) [35]—indeed can also be employed; but it needs collecting diffused light in the whole sample space and hence requires an integrating sphere, which is bulky equipment and not suitable for miniaturization into a portable device. Also, the involved modeling and the use of Monte Carlo iterations to reduce the error may be time-consuming and might be highly demanding regarding computational resources. In another method, the colloid prism method, the transmitted beam profile is measured, from which the angle of refraction is calculated using an appropriate form of Snell's law obtained by considering the forward scattering calculated from Mie theory [25]. However, this analysis is valid only for spherical particles, for which this theory can be applied. The SPR method for measuring the complex refractive index of colloids has also been reported [36,37]. Indeed, it relies on Fresnel's equation at certain points, although not in a direct way, since it is the excited

surface plasmon wave that actually interacts with the sample, rather than the reflected light beam. The dependence of the complex reflection coefficients and the phase difference on the incident angle has been considered; and indeed, the error was very small [37]. In a method called the spectral SPR, the angle of incidence is fixed while scanning the wavelength. This way one can obtain the spectral features of the liquid and avoid the mechanical components with the slow process of changing the angle of incidence with a rotation stage. However, this method requires an accurate retrieval of the phase function of the complex reflectivity [38,39], which may be not as simple or straight forward as the former methods.

In this work, a refractometry method is introduced for NP detection, which—we believe—avoids the theoretical doubts or practical difficulties of most of the previous methods, as it depends on obtaining the phase difference using spectral interferometry. The method of detecting the optical path of the coherent wave as it passes through the turbid medium has been considered more convenient to be used with colloids than those dependent on Fresnel's equations [40]. Also, the device shown—to the best of our knowledge—is the first on-chip implementation of a colloidal refractometry method. Original results obtained using this device show good agreement with the theoretically predicted values calculated using Mie scattering and the Van de Hulst formula [41]. Also, optical binding effects are reported, showing their dependence on optical power and time. This effect can be particularly useful in NP detection, as it can 'gather' the particles dispersed in the sample, even when they are few, thereby enhancing the low pollution detection capabilities.

2. Materials and Methods

2.1. Theory and Mathematical Modeling

For colloids or turbid liquids, the medium has spatial fluctuation of the refractive index. The medium is not homogeneous like normal liquids, but rather, it is heterogeneous. Such fluctuations cause scattering of the incident light, which determines the sample's turbidity. There are two principal issues: The first is the existence of an 'effective' refractive index (n_{eff}) for the colloidal material. The other is the measurement method used to determine the ERI of this sample. The ERI of a heterogeneous sample is defined in terms of the phase angle accrued by a wave propagating normally through the sample, which results from interference between forward-scattered and unscattered light [27]. When one considers a random system of scatters, with their entire possible configuration, there will be an average of the optical fields—that is the coherent component—and a diffuse component that represents the fluctuations of the optical fields from their average. Then, the coherent component is transmitted through the inhomogeneous medium with an effective propagation constant, from which the complex effective refractive index is obtained. The real part of the ERI (n_r) presents the phase lag, while the imaginary part (n_i) counts for the attenuation. This attenuation is due to the scattering loss—the part of the wave converted to the diffused component—as well as the absorption, if there is any [25]. The complex effective refractive index is then $n_{eff} = n_r - in_i$. To determine n_{eff}, the usual analytical modeling is performed by determining the forward scattering per scatterer according to its shape and size. Then, the total effect should consider the whole number of scatterers per unit volume (N) or, rather, their volume fraction (f).

2.1.1. Van de Hulst Formula

The absorbance per unit distance (δ'') for a spherical particle per radius (a) is given by:

$$\delta'' = \frac{1}{2} N C_{sca} = \frac{1}{2} N \pi a^2 Q_{sca}, \quad (1)$$

where C_{sca} is the scattering cross section per particle, and Q_{sca} is the scattering efficiency per particle. For spherical scatterers with radius a, the number of particles per unit volume can be expressed as $N = 3f/4\pi a^3$, where f is the volume fraction of the dispersion occupied by the colloidal spheres. And the absorbance then may take the form:

$$\delta'' = \frac{3f}{8a} \times Q_{sca}, \tag{2}$$

Similarly, the phase change per unit distance (δ') caused by the turbid solution is $2\pi/\lambda\left(n_{eff} - n_l\right)$, where n_l is the refractive index of the liquid medium surrounding the spheres (the continues phase), and λ is the optical wavelength in air, and is given by:

$$\delta' = \frac{3f}{8a} \times P_{sca}, \tag{3}$$

The scattering efficiency Q_{sca} is a measure of the effect of a scattering particle on diminish the amplitude of an advancing wavefront, while P_{sca} is a measure of the effect of a scattering particle on changing the phase of the advancing wavefront. Usually, the quantity $S(0)$, which is the relative complex forward-scattering amplitude per scatterer, is used in the scattering calculations. And it satisfies the following relations:

$$Q_{sca} = 4\frac{Re\{S(0)\}}{x^2} \text{ and } P_{sca} = 4\frac{Im\{S(0)\}}{x^2}, \tag{4}$$

where x is the particle size parameter and is equal to ka for a sphere of radius a, and k is the propagation constant in the liquid medium and is equal to $2\pi n_l/\lambda$.

Mie scattering provides rigorous calculations valid for any particle size parameter x to obtain the scattering amplitude $S(0)$. But sometimes it is not easy to compute. So, some approximations have been derived for certain cases: Rayleigh scattering describes the region where the particles are much smaller than the optical wavelength, i.e., $x \ll 1$. In this case, they can be modeled as a point optical dipole. Rayleigh–Gans (RG) scattering describes a region of arbitrary x, but with small phase shift caused by the particle, i.e., $x(m-1) \ll 1$, where m is the refractive index of the particle relative to that of the surrounding liquid medium n_p/n_l, with n_p being the refractive index of the particle's material. For particles large enough for ray optics and diffraction to be applied, the anomalous diffraction (AD) approximation is valid. More details about these approximations can be found in Ref. [42]. In the intermediate cases, the regions of validity of the RG and AD approximations overlap. Hence, Mie scattering should be used. The Mie scattering model gives an exact analytical expression for the scattering from an isotropic sphere. The accuracy is limited by the computation only, for instance, how many terms are employed to express the infinite series. Mie theory states that [41]:

$$S(0) = \frac{1}{2}\sum_{n-1}^{\infty}(2n+1)(a_n + b_n), \tag{5}$$

where a_n and b_n are the Mie coefficients, and they can be found in Ref. [41]. Generally, these coefficients are complex, allowing the calculation of Q_{sca} and P_{sca} from Equation (4). Many calculations and codes have been developed to obtain these Mie parameters and are available in the literature [43,44].

The effective complex refractive index n_{eff} is then obtained from the Van de Hulst formula [17,42,44]:

$$n_{eff} = n_r - in_i = n_l + \frac{2\pi n_l N}{ik^3} \times S(0), \tag{6}$$

An important note is that the Van de Hulst formula is employed in the case of independent scatterers, where no multi-scattering occurs. This is usually the case for diluted colloidal solutions. But the limit of their volume fraction is not agreed upon in the literature. Keith Alexander et al. stated that "The division between dilute and concentrated dispersions occurs at volume fractions of approximately 0.01", but that limit could be extended by performing the measurements on a thin layer of dispersion to avoid multiple scattering problems, yielding acceptable fitting with volume fractions up to 0.5 for particle size parameter, x, up to 7.65 [18]. Meanwhile, Augusto García-Valenzuela et al. showed that the Van de Hulst formula can be used with acceptable precision for the measurements of colloids with volume fraction up to 0.05 for size parameters up to 20.16 [40].

2.1.2. Non-Local Effective-Medium Approach

When the effective permittivity (ε_{eff}) and, also the effective permeability (μ_{eff}) if any, depend on the wave vector of the electromagnetic fields propagating in the medium, in addition to the dependence on frequency, this means the behavior of the electromagnetic response is spatially dispersive. Non-local effects are important to consider usually when the particles are big enough or close enough for the exciting electromagnetic field to vary within them [40]. Turbid colloidal medium fits that description and should hence be modeled by this approach, especially when the medium is dense, i.e., has rather a high volume fraction, and/or the particle size parameter is large. In this case, the Van de Hulst formula gives poor fitting, and the effective complex refractive index n_{eff} behavior versus the volume fraction exceeds the linear region. For evaluating the effective refractive index by this approach, the following formula is employed:

$$n_{eff}(\omega) = n_l(\omega)\left(1 + 2i\frac{3f}{2x^3}S(0)\right)^{1/2}, \quad (7)$$

It is worth noting that expanding the square root into an infinite serious and then taking the approximation up to the second term leads to the Van de Hulst formula for the effective refractive index. It can represent the approximation of the linear region.

2.2. Experimental Setup

As stated before, our proposed method is categorized under the phase difference interferometry methods. It depends on measuring the interference spectrum of a silicon Fabry–Pérot integrated cavity with curved surfaces. The schematic of the device is introduced in Figure 1. The two cylindrical Bragg mirrors form the cavity, which achieves multiple reflections of the light at certain wavelengths corresponding to resonance. The capillary tube in between holds the colloidal solution under test, whose refractive index introduces phase change to the light wave passing through, appearing as a wavelength shift in the cavity resonance. The curvature of the mirrors and the tube serves a great job in realizing stability of the cavity with a Gaussian input beam, despite its long physical length (above 250 μm). That is, the Gaussian beam expands along its propagation; hence, it will finally escape the cavity, causing (diffraction loss) if straight surfaces are to be employed, as in previous trials reported in the literature [45–51]. But with curved surfaces, the Gaussian beam is confined inside the cavity, reducing the diffraction loss and increasing the quality factor (Q) to over 1100. Hence, it could stand the scattering loss from the colloidal particles without causing the interference peaks to vanish. The cylindrical mirrors achieve confinement in the horizontal plan, while the capillary tube with liquid inside confine the light in the vertical plan. Detailed analytical and numerical studies of this cavity have been formerly performed and presented in previous publications [52,53].

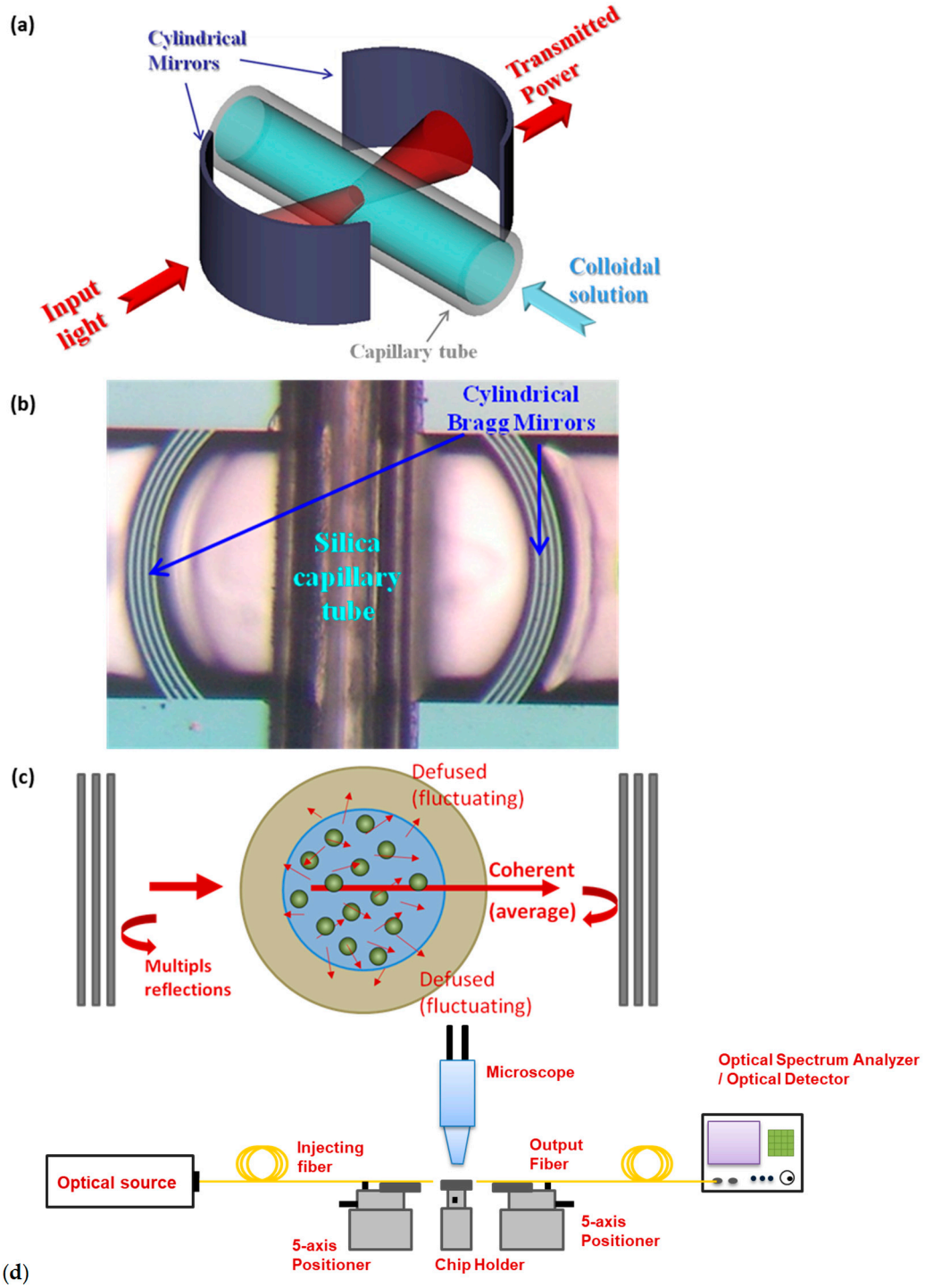

Figure 1. (**a**) A 3D schematic diagram of the optofluidic Fabry–Pérot resonator with the micro-capillary tube inside. (**b**) Photograph of the corresponding fabricated device used for the experiments. (**c**) Cross-section schematic view illustrating the different components of light inside the cavity filled with suspended particles acting as light scatterers. (**d**) Schematic of the experimental setup indicating the main key devices.

The cavities are realized on a silicon chip fabricated using the improved Deep Reactive Ion Etching (DRIE) process to form trenches on a silicon substrate with depth over 70 μm, enabling hosting the capillary tube and the fibers. The cylindrical Bragg mirrors have three or four silicon/air bilayers, with a radius of curvature R = 140 μm. The Bragg mirrors' silicon layers have a thickness of 3.67 μm (the thickness that the light beam propagates through, as shown in Figure 1a. But this thickness appears as a lateral dimension if seen

from top view, as in Figure 1b), while the Bragg mirrors' air gabs have a thickness of 3.49 μm; both thicknesses correspond to an odd multiple of quarter the central wavelength—which is 1550 nm—in silicon and in air, respectively. Then, a fused silica micro-tube with an outer diameter of 128.1 ± 1.2 μm and an inner diameter of 75.3 ± 1.2 μm (from Polymicro Technologies, Lisle, IL, USA, with part number TSP075150) is placed between the mirrors and is connected with an external larger-diameter tube to allow injecting the colloidal solution, which is formed by deionized water (DI water) containing 0.5 μm polystyrene microspheres (reference 17152 from Polysciences, Hirschberg, Germany) with different concentration values that will be indicated with each experiment. There were no pre-preparations for the colloidal solution except mixing the required amount of the solution containing the beads provided by the vendor with the proper amount of DI water to reach the intended concentration and then shaking a little by hand. The light is injected and detected using either one of two setups: a swept-wavelength tunable laser source (model 81949A from Agilent, Santa Clara, CA, USA) in the near-infrared covering the L and C bands, with a power meter (model 81634B from Agilent) as a detector of the transmitted power; or by using a superluminescence light-emitting diode (SLED) as a wideband source (model S5FC1005S from Thorlabs, Bergkirchen, Germany), with an optical spectrum analyzer (model MS9710B from Anritsu, Kanagawa, Japan) to obtain the spectrum of the transition band. The first setup can afford a smaller wavelength step and hence a better resolution; but it necessitates changing the light wavelength step by step and detecting the corresponding power until scanning the entire band, i.e., the spectrum is drawn point by point. The second setup can obtain the spectrum at a single shoot; hence, it is faster and avoids temporal noise and variations, as will be presented in the results; however, it has lower spectral resolution. The equipment is controlled via a computer using a GPIB interface card to synchronize the injection and the acquisition of the proper input and output light waves. The setup is connected using single-mode (SM) fibers. The light is coupled into/from the cavity with ordinary cleaved fibers glued to the chip in order to minimize the vibration disturbances. In some experiments, lensed fibers from Corning, with spot size of 18 μm and 300 μm working distance, are used instead, which affects the performance as will be indicated. Five axis positioners are used to align each fiber in the input and output grooves on the chip, while the sample holder is mounted on a two-axis positioner. All elements are mounted on an optical table to reduce vibration effects. The system is observed under a stereo microscope, and the results were recorded by a C-Mount CMOS camera attached to the microscope (from Olympus, Nagano, Japan).

3. Results and Discussion

3.1. Colloidal Refractometry

The first experiment is performed by injecting a solution of DI water with and without beads. The concentration of the particles is between 0.34% and 2.5% solid content with respect to volume (w/v). This is equivalent to concentrations of 6.27×10^{10} particles/mL and 3.64×10^{11} particles/mL, respectively. The setup employs the tunable laser and the power meter to inject and record their spectra via a couple of cleaved fibers glued to the chip. Figure 2a presents the spectrum of the DI water and the spectra of the turbid solution with beads having different concentration. As can be noticed, the spectrum shifts upon changing the solid contents. The resonance happens at higher wavelengths for higher bead concentration as the polystyrene has higher refractive index than the DI water, which is 1.574 at near-infrared range. Hence, the effective refractive index will be higher. Also, the spectrum has a lot of perturbations, as compared with the spectrum of DI water free from particles. These perturbations are temporally varying and are expectedly due to the Brownian motions of the beads. These perturbations are less for

lower particle concentrations. The observation of the interference peaks in the spectra is enough proof of having a proper coherent component of the light despite the large scattering or diffused portion due to the medium turbidity. Hence, this coherent wave can be used to detect n_{eff}, which is defined for this component only, as presented earlier. The wavelength shift corresponding to each solution at a given bead concentration is determined from its spectrum as compared to the DI water spectrum, which is taken as a reference. This processing is not straight forward due to the non-smooth shape of the spectra, which necessitates post processing.

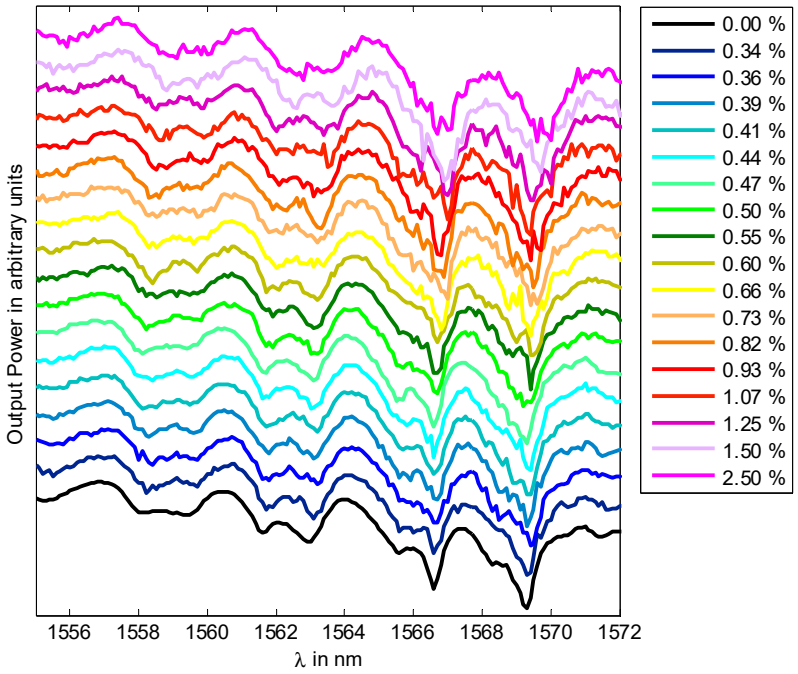

(**a**)

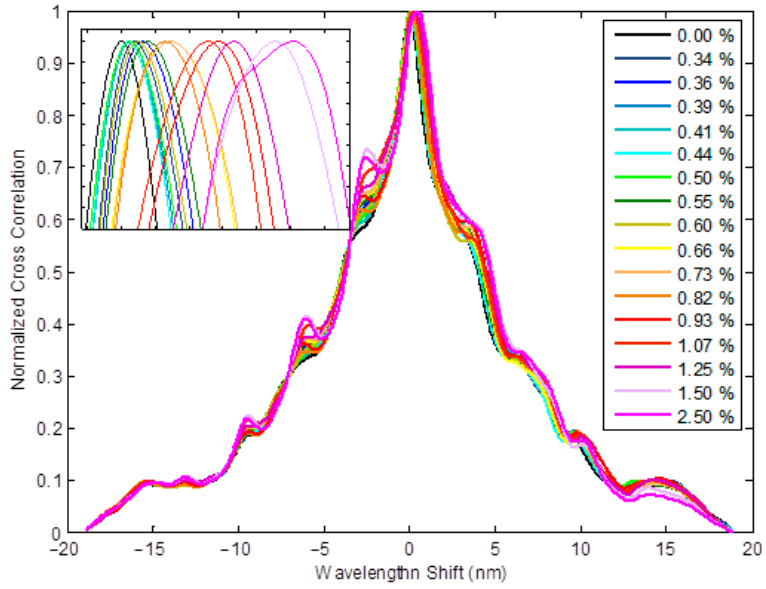

(**b**)

Figure 2. (**a**) The spectra of DI water (0.00%) and DI water containing 0.5 µm polystyrene microspheres with different concentrations ranging from 2.5% to 0.34% solids (w/v). Note that the power reference has been changed for every curve in order to superpose them for better comparison. (**b**) The normalized interpolated cross-correlation functions for different bead concentrations are correlated to the DI water. The black curve (0.00%) is the autocorrelation of the DI water spectrum taken as a reference and of course has its maximum at zero shift. The inset shows a zoomed view of the peak area.

The cross-correlation technique is employed to accurately extract the spectral wavelength shift corresponding to changes in bead concentration. First, each spectrum is cross-correlated with the curve of the pure DI water, which is taken as a reference. This cross-correlation function is then normalized to its maximum and interpolated to have a better resolution. Cross-correlation measures the similarity between two signals as a function of a shift applied to one of them. Hence, that function has a maximum value at the shift where the two correlated spectra have maximum 'similarity', despite any noise or pondering in the spectral peaks. Figure 2b shows the wavelength shift ($\Delta\lambda$) obtained using the explained technique.

From these values, the effective refractive index of the colloidal solution (n_{eff}) can be finally obtained from Equation (8):

$$\mathrm{Re}\left(n_{eff}\right) = \mathrm{Re}(n_{water}) + \frac{\Delta\lambda}{\mathrm{Sensitivity}}, \tag{8}$$

where Sensitivity = 84.3 nm/RIU for the used device, and n_{water} = 1.3167 at the employed wavelength range. The device sensitivity was characterized by measuring the spectral shift using two homogeneous liquids with known refractive indices, which are DI water and acetone. Figure 3 shows the effective refractive index values obtained from the measured spectral shifts.

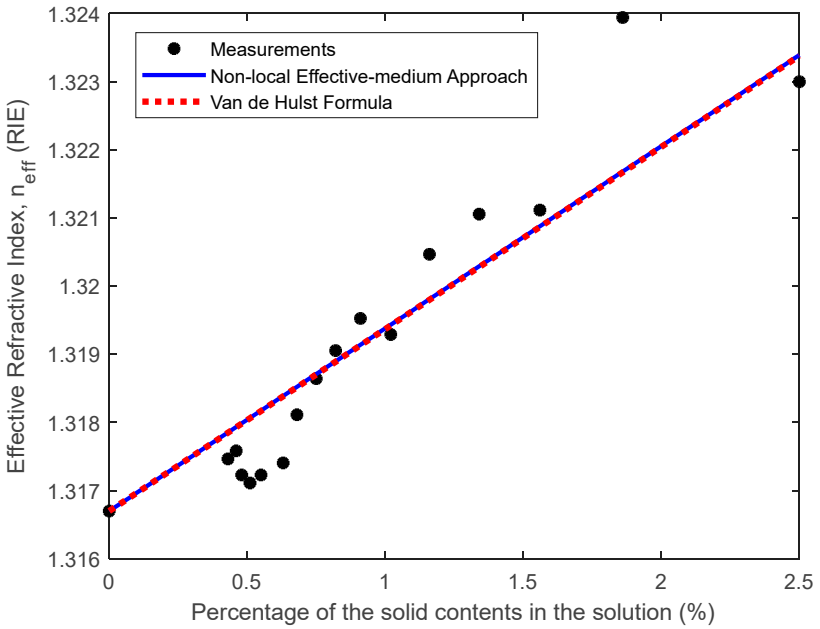

Figure 3. Measured refractive index of the turbid solution compared to the theoretical prediction using both non-local effective-medium approach and Van de Hulst approximation models.

To provide a theoretical prediction for the trend of the effective refractive index, both non-local effective-medium approach and Van de Hulst approximation are employed and compared. For our case, the particle size parameter x = 1.3228 is rather small, and the volume fraction is less than 0.025; hence, the two approaches are expected to give similar results. This is indeed the case, as shown in Figure 3, which presents the plots of Equations (6) and (7). For obtaining the complex forward-scattering amplitude per particle, $S(0)$, the rigorous Mie scattering has to be involved since the particle sizes are not very small compared to the wavelength. For our size parameter, $S(0) = 0.0344 - 0.3144i$, as obtained from Mie calculations [44]. It is worth noting that the particles we used are rather

'large' in the nanoscale (500 nm). For nanoparticles with small size compared to the optical wavelength, i.e., with $x \ll 1$, Rayleigh scattering can be used, as detailed in Section 2.1.

It is worth considering that the employed stable Fabry–Pérot cavity could stand the scattering loss from the sample turbidity while still providing a high quality factor. The quality factor of the peaks near λ = 1564 nm from the different concentration curves are calculated from Figure 2a after smoothing the curves by averaging each five successive points to have a better shape of the peak free from noise. As expected, the Q-factor values decrease with increasing scattering loss at higher bead concentrations; but it is always sufficiently high, as it decreases only from about 1280 to about 1108. This emphasizes the importance of our novel design of the Fabry–Pérot cavity, based on curved surfaces, which can attain such high values of the Q-factor, thereby tolerating scattering loss from the colloidal particles without causing the interference peaks to diminish severely or even vanish completely. For the usual Fabry–Pérot cavities employing straight mirrors found in the literature, one can only find much lower values of quality factor, at the level of Q = 400, even with homogeneous liquids without turbidity [46]. These values are expected to be lower if colloidal liquids are to be introduced inside the cavity, which might result in infeasible spectrum with non-resolvable peaks. Therefore, normal Fabry–Pérot cavities with low quality factors are not recommended for lossy media.

3.2. Particles Aggregation

In another experiment, when the lensed fiber is used to inject light into the cavity instead of the ordinary cleaved fiber, an interesting phenomenon is observed. As shown in Figure 4, the particles tend to accumulate or aggregate solely with the effect of light. This phenomenon has been attributed to the optical binding effect that is—somehow—a type of optical trapping phenomenon [54–57]. With the existence of particles within an optical field, the light gets scattered on such particles. At sufficiently high light intensity, the optical scattering force effects—or sometimes known as optical radiation pressure—are pronounced. The re-scattered light on the particles creates mutual optical forces amongst them, causing their motion and hence redistribution of the field until a new force equilibrium is attained. Note that, the light beam injected using a lensed fiber is expected to have a better confinement, and hence higher levels of intensity compared to ordinary cleaved fibers, where such effects were not observed upon using them in the previous section. So, if a colloidal suspension is to be optically characterized only, a cleaved bare fiber should be used, while in the case of desiring to achieve the aggregation process, lensed fibers should be employed to achieve the optical binding effect. This particle accumulation behavior might be useful in speeding up the colloid gelling or coagulation process in some industries. This process increases with input light power, as presented in Figure 4. When a fixed laser wavelength is injected using a lensed fiber, the particles gather over time in the middle area of the cavity illuminated by light. After the same time period, the particles' population is higher when a higher laser source power is injected. The indicated photos in Figure 5 were taken 20 min after starting the laser source at different powers ranging from 4 mW to 30 mW. The same effect occurs no matter which input wavelength is used, whether on cavity resonance or not. It is worth noting that this is a reversible process, i.e., upon switching off the light, the particles diffuse randomly over a certain time constant.

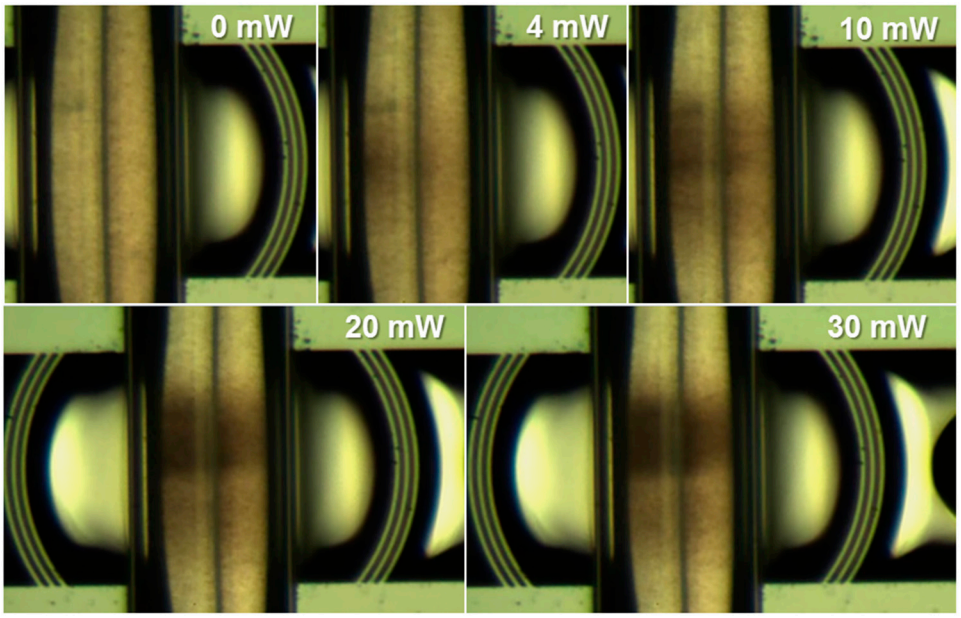

Figure 4. The accumulation of 0.5 μm microspheres (initial concentration = 6.27×10^{10} particles/mL) after 20 min at different laser source powers.

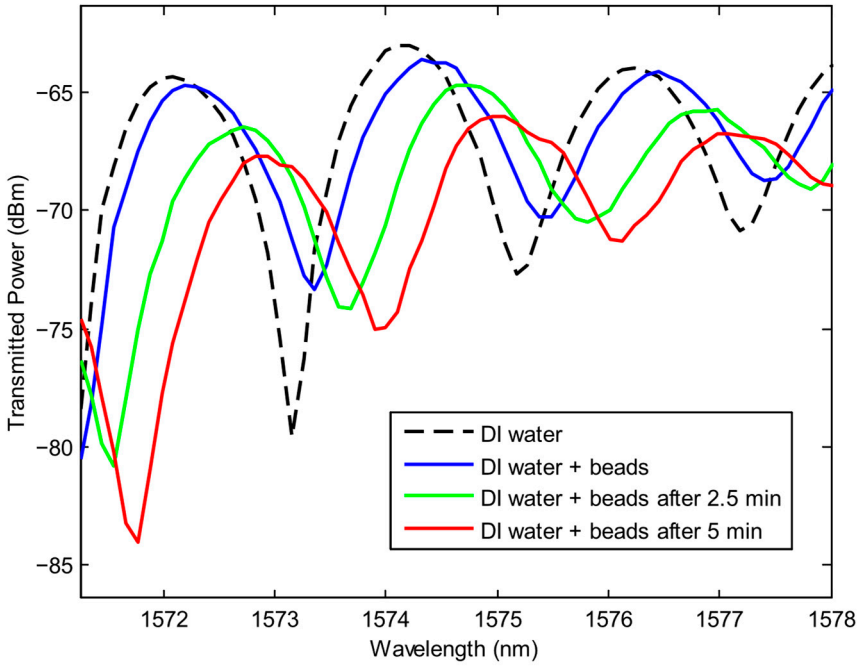

Figure 5. The spectra of DI water and DI water containing 0.5 μm polystyrene microspheres at different time intervals along the aggregation process.

To characterize the particle accumulation process over time, the effective refractive index is measured simultaneously while achieving aggregation. This is achieved by using a laser source at a selected wavelength to achieve optical binding, while using a broadband SLED source to have a wide spectrum for refractometry. The two source inputs are coupled together using a fiber coupler and then injected to the cavity through a lensed fiber. The transmission spectrum is analyzed by the optical spectrum analyzer and is recorded via a computer every several minutes along the aggregation process. Figure 5 shows selected curves amongst such spectra, along with the reference curve of DI water. At first glance, one can notice that the trend is moving forward with time evolution and the transmitted power is decreased. This is expected, as the scattering losses increase with the particles' gathering.

From another perspective, these curves are perturbation-free, unlike those presented in Figure 2a, which were obtained by a tunable laser and a detector. This is because of the fast acquisition of the spectrum at almost a single moment, so that the Brownian motion does not get enough time to change the particle distribution 'seen' or encountered by the light wave.

The spectral shifts in the different curves from the reference DI water curve are calculated using the aforementioned cross-correlation technique. The normalized cross-correlation functions are presented in Figure 6. The function has a maximum value at the lag where both spectra are mostly similar; hence, this lag is a direct measure of the spectral shift between them. The inset in Figure 6 shows a zoomed view around these maxima to indicate the shifts in the different curves. It is evident that the shift increases with time, emphasizing an increasing accumulation of the beads over time, which reflects on the effective refractive index and, consequently, the phase difference in the spectra.

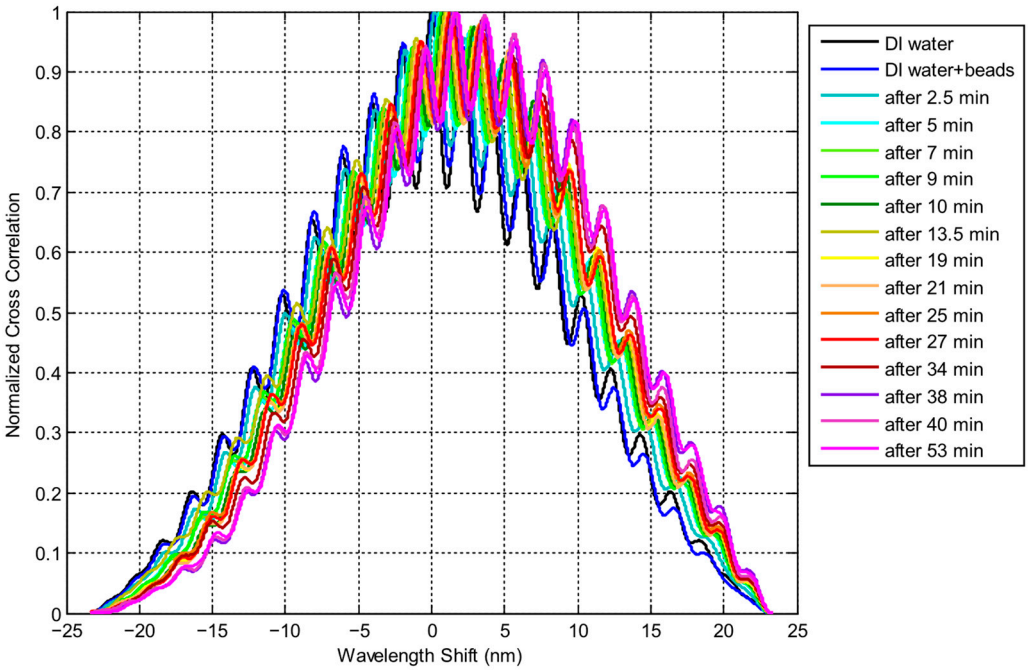

Figure 6. Normalized, interpolated cross-correlation functions for the spectra at different times along the aggregation process, correlated to the DI water spectrum. The black curve is the autocorrelation of the DI water spectrum, taken as a reference, and of course has its maximum at a zero shift. The inset is a zoomed view around the peak area, indicating the spectral shifts between the curves.

From the spectral shift obtained from Figure 6, the effective refractive index can be calculated knowing the sensitivity, as previously pointed out. Such effective refractive index values are plotted on the right-side y-axis in Figure 7. Using Equation (3), the volume fraction of the beads, or their solid contents inside the solution, is evaluated and plotted on the left-side y-axis of Figure 7. It is worth noting that, for these measurements, the points' deviation from the fitting curve is much smaller than in the previous case recorded using the tunable laser and detector, since the noise and perturbation are much lower, as explained above, which enables obtaining more accurate measurements. The indicated quantities have been fitted by a suitable function. They have been found to be proportional to the time to the power 0.5 ($\propto t^{0.5}$). This power-law (with different exponents dependent on experimental conditions) is known for particle aggregation behavior [58]. And the specific 0.5 exponent has been related to Electro-Rheological fluids [59]. The matching of measured volume fraction and effective refractive index is rather perfect. This similarity might suggest the same underlining physics of particle polarization and dipole formation

under the electric field. Of course, further investigation is required before confirming or denying this hypothesis. But until that happens, this phenomenon has a practical usefulness in detecting the presence of NPs in the samples under test—even when they are scarce—due to their aggregation by light.

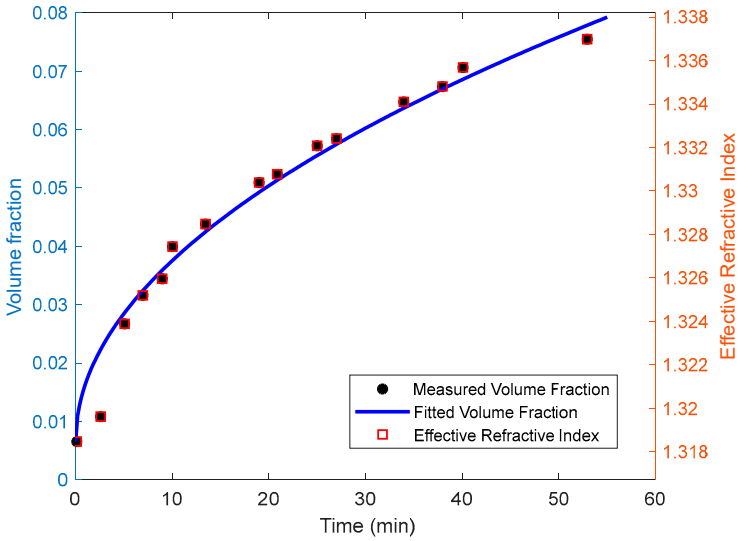

Figure 7. The effective refractive index (right-side y-axis) and the percentage of the solid contents in the solution (left-side y-axis) of the aggregation process over time.

4. Conclusions

In this article, we have discussed an on-chip technique employed for measuring the effective refractive index for NPs colloidal or turbid liquids. Unlike some previous techniques in the literature that was deemed unsuitable for heterogeneous liquids like colloids, this one is based on measuring the phase delay and thereby agreed upon to be suitable for colloids. An optofluidic Fabry–Pérot microresonator with curved surfaces is used to measure the spectral shift in different concentrations of NPs in aqueous solution. The curved surfaces achieves high quality factor, which enables overcoming the scattering losses from the particles. The measurements show acceptable consistency with the theoretically calculated values.

On another aspect, using light in resonance might produce high intensity in some cases, which leads to particle aggregation or binding. This interesting phenomenon might be useful in detecting even a few NPs in low-concentration samples, enabling better sensing resolution.

Author Contributions: N.G. was responsible for primary manuscript preparation, experimental work, and analytical modeling and calculations. F.M. fabricated the chips. E.R. participated in the analytical modeling and calculations, supervised, and revised the work. T.B. provided the device structure and characterization idea and the work concept, facilitated the process, and supervised the work. All authors have read and agreed to the published version of the manuscript.

Funding: This research received no external funding.

Data Availability Statement: The raw data supporting the conclusions of this article will be made available by the authors on request.

Conflicts of Interest: The authors declare no conflicts of interest.

References

1. Lehner, R.; Weder, C.; Petri-Fink, A.; Rothen-Rutishauser, B. Emergence of nanoplastic in the environment and possible impact on human health. *Environ. Sci. Technol.* **2019**, *53*, 1748–1765. [CrossRef]
2. Winiarska, E.; Jutel, M.; Zemelka-Wiacek, M. The potential impact of nano- and microplastics on human health: Understanding human health risks. *Environ. Res.* **2024**, *251*, 118535. [CrossRef]
3. Ding, Y.; Tang, S.; Zhang, T.; Ma, S.; Xu, H.; Zhao, Y. Unveiling the Environmental Characteristics of Sub-1000-nm Nanoplastics: A Comprehensive Review of the Preparation Methods for Nanoplastic Model Samples. *Environ. Sci. Technol.* **2025**, *59*, 18391–18410. [CrossRef]
4. Thompson, R.C.; Courtene-Jones, W.; Boucher, J.; Pahl, S.; Raubenheimer, K.; Koelmans, A.A. Twenty years of microplastic pollution research—What have we learned? *Science* **2024**, *386*, eadl2746. [CrossRef]
5. Gigault, J.; Ter Halle, A.; Baudrimont, M.; Pascal, P.Y.; Gauffre, F.; Phi, T.L.; El Hadri, H.; Grassl, B.; Reynaud, S. Current opinion: What is a nanoplastic? *Environ. Pollut.* **2018**, *235*, 1030–1034. [CrossRef] [PubMed]
6. Wu, R.; Hao, L.; Tian, H.; Liu, J.; Dong, C.; Xue, J. Qualitative Discrimination and Quantitative Prediction of Microplastics in Ash Based on Near-Infrared Spectroscopy. *J. Hazard. Mater.* **2024**, *469*, 133971. [CrossRef] [PubMed]
7. Schmidt, J.; Haave, M.; Underhaug, J.; Wang, W. Unlocking the Potential of NMR Spectroscopy for Precise and Efficient Quantification of Microplastics. *Micropl. Nanopl.* **2024**, *4*, 17. [CrossRef]
8. Kutralam-Muniasamy, G.; Shruti, V.C.; Pérez-Guevara, F.; Flores, J.A. The Emerging Field of Inductively Coupled Plasma Mass Spectrometry for (Micro)Nanoplastic Analysis: "The 3As" Analysis, Advances, and Applications. *TrAC Trends Anal. Chem.* **2024**, *174*, 117673. [CrossRef]
9. Rodríguez-Quiroz, O.; Luna-Moreno, D.; Sánchez-Álvarez, A.; Quintanilla-Villanueva, G.E.; Silva-Hernández, O.J.; Rodríguez-Delgado, M.M.; Villarreal-Chiu, J.F. Measurement of the Effective Refractive Index of Suspensions Containing 5 µm Diameter Spherical Polystyrene Microparticles by Surface Plasmon Resonance and Scattering. *Chemosensors* **2025**, *13*, 257. [CrossRef]
10. Costa, C.Q.V.; Cruz, J.; Martins, J.; Teodósio, M.A.A.; Jockusch, S.; Ramamurthy, V.; Da Silva, J.P. Fluorescence sensing of microplastics on surfaces. *Environ. Chem. Lett.* **2021**, *19*, 1797–1802. [CrossRef]
11. Ludescher, D.; Wesemann, L.; Schwab, J.; Karst, J.; Sulejman, S.B.; Ubl, M.; Clarke, B.O.; Roberts, A.; Giessen, H.; Hentschel, M. Optical sieve for nanoplastic detection, sizing and counting. *Nat. Photon.* **2025**, *19*, 1138–1145. [CrossRef]
12. Schwaferts, C.; Sogne, V.; Welz, R.; Meier, F.; Klein, T.; Niessner, R.; Elsner, M.; Ivleva, N.P. Nanoplastic Analysis by On-line Coupling of Raman Microscopy and Field-Flow Fractionation Enabled by Optical Tweezers. *Anal. Chem.* **2020**, *92*, 2682–2689. [CrossRef]
13. Xie, J.; Gowen, A.; Xu, W.; Xu, J. Analysing Micro-and Nanoplastics with Cutting-Edge Infrared Spectroscopy Techniques: A Critical Review. *Anal. Methods* **2024**, *16*, 2177–2197. [CrossRef] [PubMed]
14. Tsuchida, K.; Imoto, Y.; Saito, T.; Hara, J.; Kawabe, Y. A Novel and Simple Method for Measuring Nano/Microplastic Concentrations in Soil Using UV-Vis Spectroscopy with Optimal Wavelength Selection. *Ecotoxicol. Environ. Saf.* **2024**, *280*, 116366. [CrossRef]
15. Peiponen, K.-E.; Räty, J.; Ishaq, U.; Pélisset, S.; Ali, R. Outlook on optical identification of micro- and nanoplastics in aquatic environments. *Chemosphere* **2019**, *214*, 424–429. [CrossRef]
16. Jääskeläinen, A.J.; Peiponen, K.-E.; Räty, J.A. On Reflectometric Measurement of a Refractive Index of Milk. *J. Dairy Sci.* **2001**, *84*, 38–43. [CrossRef]
17. Mohammadi, M. Colloidal refractometry: Meaning and measurement of refractive index for dispersions; the science that time forgot. *Adv. Colloid Interface Sci.* **1995**, *62*, 17–29. [CrossRef]
18. Alexander, K.; Killey, A.; Meeten, G.H.; Senior, M. Refractive index of concentrated colloidal dispersions. *J. Chem. Soc. Faraday Trans. 2* **1981**, *77*, 361–370. [CrossRef]
19. Zilio, S.C. A simple method to measure critical angles for high-sensitivity differential refractometry. *Opt. Express* **2012**, *20*, 1862–1867. [CrossRef] [PubMed]
20. Zhu, X.; Fryd, M.M.; Huang, J.-R.; Mason, T.G. Optically probing nanoemulsion compositions. *Phys. Chem. Chem. Phys.* **2012**, *14*, 2455–2461. [CrossRef]
21. Azzam, R.M.A. Maximum minimum reflectance of parallel-polarized light at interfaces between transparent and absorbing media. *J. Opt. Soc. Am.* **1983**, *73*, 959–962. [CrossRef]
22. Kim, S.Y.; Vedam, K. Analytic solution of the pseudo-Brewster angle. *J. Opt. Soc. Am. A* **1986**, *3*, 1772–1773. [CrossRef]
23. Azzam, R.M.A.; Ugbo, E.E. Angular range for reflection of p-polarized light at the surface of an absorbing medium with reflectance below that at normal incidence. *J. Opt. Soc. Am. A* **2002**, *19*, 112–115. [CrossRef]
24. Champion, J.V.; Meeten, G.H.; Senior, M. Refractive index of particles in the colloidal state. *J. Chem. Soc. Faraday Trans. 2* **1978**, *74*, 1319–1328. [CrossRef]
25. Reyes-Coronado, A.; García-Valenzuela, A.; Sánchez-Pérez, C.; Barrera, R.G. Measurement of the effective refractive index of a turbid colloidal suspension using light refraction. *New J. Phys.* **2005**, *7*, 89. [CrossRef]

26. Barrera, R.G.; Reyes-Coronado, A.; García-Valenzuela, A. On the effective response of colloidal systems. *Phys. Rev. B* **2007**, *75*, 184202. [CrossRef]
27. Meeten, G.H. Refractive index errors in the critical-angle and the Brewster-angle methods applied to absorbing and heterogeneous materials. *Meas. Sci. Technol.* **1997**, *8*, 728–733. [CrossRef]
28. Niskanen, I.; Räty, J.; Peiponen, K.-E. Complex refractive index of turbid liquids. *Opt. Lett.* **2007**, *32*, 862–886. [CrossRef] [PubMed]
29. Calhoun, W.R.; Maeta, H.; Combs, A.; Bali, L.M.; Bali, S. Measurement of the refractive index of highly turbid media. *Opt. Lett.* **2010**, *35*, 1224–1226. [CrossRef] [PubMed]
30. Dong, M.L.; Goyal, K.G.; Worth, B.W.; Makkar, S.S.; Calhoun, W.R.; Bali, L.M.; Bali, S. Accurate in situ measurement of complex refractive index and particle size in intralipid emulsions. *J. Biomed. Opt.* **2013**, *18*, 087003. [CrossRef]
31. Goyal, K.G.; Dong, M.L.; Kane, D.G.; Makkar, S.S.; Worth, B.W.; Bali, L.M.; Bali, S. Note: Refractive index sensing of turbid media by differentiation of the reflectance profile: Does error-correction work? *Rev. Sci. Instrum.* **2012**, *83*, 086107. [CrossRef]
32. Ma, X.; Lu, J.Q.; Brock, R.S.; Jacobs, K.M.; Yang, P.; Hu, X.-H. Determination of complex refractive index of polystyrene microspheres from 370 to 1610 nm. *Phys. Med. Biol.* **2003**, *48*, 4165–4177. [CrossRef]
33. Shybanov, E.B.; Haltrin, V.I. Modeling the Effective Refractive Index and Absorption Coefficient of a Turbid Medium with Polydisperse Particles. In Proceedings of the Oceans 2002. MTS/IEEE Conference, Biloxi, MS, USA, 29–31 October 2002; IEEE: Piscataway, NJ, USA, 2003; pp. 1968–1974.
34. Jacques, S.L. Optical properties of biological tissues: A review. *Phys. Med. Biol.* **2013**, *58*, R37–R61. [CrossRef]
35. Kaplan, P.D.; Dinsmore, A.D.; Yodh, A.G.; Pine, D.J. Diffuse-transmission spectroscopy: A structural probe of opaque colloidal mixtures. *Phys. Rev. E* **1994**, *50*, 4827–4835. [CrossRef]
36. Alexandre, K.; Paul, D.G.; Hans, A.S. Effective refractive index and absorption of concentrated latex dispersions. *Appl. Opt.* **2000**, *39*, 3314–3322.
37. Yingying, Z.; Jiancheng, L.; Cheng, Y.; Zhenhua, L. Determination of effective complex refractive index of a turbid liquid with surface plasmon resonance phase detection. *Appl. Opt.* **2009**, *48*, 1262–1267. [CrossRef]
38. Saarinen, J.J.; Vartiainen, E.M.; Peiponen, K.-E. Retrieval of the complex permittivity of spherical nanoparticles in a liquid host material from a spectral surface plasmon resonance measurement. *Appl. Phys. Lett.* **2003**, *83*, 893–895. [CrossRef]
39. Erik, M.V.; Jarkko, J.S.; Peiponen, K.E. Method for extracting the complex dielectric function of nanospheres in a water matrix from surface-plasmon resonance data. *J. Opt. Soc. Am. B* **2005**, *22*, 1173–1178. [CrossRef]
40. García-Valenzuela, A.; Barrera, R.G.; Gutiérrez-Reyes, E. The effective refractive index of turbid colloidal suspensions. *Opt. Express* **2008**, *16*, 19741–19746. [CrossRef] [PubMed]
41. Van de Hulst, H.C. *Light Scattering by Small Particles*; John Wiley: New York, NY, USA, 1957.
42. Meeten, G.H. Refraction by spherical particles in the intermediate scattering region. *Opt. Commun.* **1997**, *134*, 233–240. [CrossRef]
43. Champion, J.V.; Meeten, G.H.; Senior, M. Refraction by spherical colloid particles. *J. Colloid Interface Sci.* **1979**, *72*, 471–482. [CrossRef]
44. Champion, J.V.; Meeten, G.H.; Senior, M. Optical turbidity and refraction in a dispersion of spherical colloidal particles. *J. Chem. Soc. Faraday Trans. 2* **1979**, *75*, 184–194. [CrossRef]
45. Domachuk, P.; Littler, I.; Cronin-Golomb, M.; Eggleton, B. Optofluidic refractive index sensor. *Appl. Phys. Lett.* **2006**, *88*, 093513. [CrossRef]
46. Song, W.Z.; Zhang, X.M.; Liu, A.Q.; Lim, C.S.; Yap, P.H.; Hosseini, H.M.M. Refractive index measurement of single living cells using on-chip Fabry-Pérot cavity. *Appl. Phys. Lett.* **2006**, *89*, 203901. [CrossRef]
47. Chin, L.K.; Liu, A.Q.; Lim, C.S.; Zhang, X.M.; Ng, J.H.; Hao, J.Z.; Takahashi, S. Differential single living cell refractometry using grating resonant cavity with optical trap. *Appl. Phys. Lett.* **2007**, *91*, 243901. [CrossRef]
48. Shao, H.; Wang, W.; Lana, S.; Lear, K. High-Q tunable photonic crystal microcavity with integrated liquid-crystal infiltration and heater for high-sensitivity refractive index sensing. *IEEE Photonics Technol. Lett.* **2008**, *20*, 493–495. [CrossRef]
49. Chin, L.K.; Liu, A.Q.; Lim, C.S.; Lin, C.L.; Ayi, T.C.; Yap, P.H. An optofluidic volume refractometer using Fabry–Pérot resonator with tunable liquid microlenses. *Biomicrofluidics* **2010**, *4*, 024107. [CrossRef]
50. Wang, W.; Kisker, D.W.; Thamm, D.H.; Shao, H.; Lear, K.L. A high-throughput single-cell refractometer for monitoring cellular behavior. *IEEE Trans. Biomed. Eng.* **2011**, *58*, 853–859. [PubMed]
51. St-Gelais, R.; Masson, J.; Peter, Y.-A. Integrated Fabry–Pérot cavity based on SU-8 polymer for optofluidic sensing. *Appl. Phys. Lett.* **2009**, *94*, 243905. [CrossRef]
52. Malak, M.; Pavy, N.; Marty, F.; Peter, Y.-A.; Liu, A.Q.; Bourouina, T. Micromachined Fabry–Perot resonator combining submillimeter cavity length and high quality factor. *Appl. Phys. Lett.* **2011**, *98*, 211113. [CrossRef]
53. Malak, M.; Gaber, N.; Marty, F.; Pavy, N.; Richalot, E.; Bourouina, T. Analysis of Fabry-Perot optical micro-cavities based on coating-free all-Silicon cylindrical Bragg reflectors. *Opt. Express* **2013**, *21*, 2378–2383. [CrossRef]
54. Burns, M.M.; Fournier, J.; Golovchenko, J.A. Optical binding. *Phys. Rev. Lett.* **1989**, *63*, 1233–1236. [CrossRef] [PubMed]

55. Gaber, N.; Malak, M.; Marty, F.; Angelescu, D.E.; Richalot, E.; Bourouina, T. Particles Optical Trapping and Binding in Optofluidic Stable Fabry–Pérot Resonator with Single-Sided Injection. *Lab Chip* **2014**, *14*, 2259–2265. [CrossRef] [PubMed]
56. Bowman, R.W.; Padgett, M.J. Optical trapping of a microscopic sphere in a standing-wave optical field. *Rep. Prog. Phys.* **2013**, *76*, 026401. [CrossRef]
57. Brzobohatý, O.; Čižmár, T.; Karásek, V.; Šiler, M.; Dholakia, K.; Zemánek, P. Experimental and theoretical determination of optical binding forces. *Opt. Express* **2010**, *18*, 25389–25402. [CrossRef] [PubMed]
58. Xia, H.; Pang, R.Y.; Zhang, R.; Miao, C.X.; Wu, X.Y.; Hou, X.S.; Zhong, C. Study of colloidal particle Brownian aggregation by low-coherence fiber optic dynamic light scattering. *J. Colloid Interface Sci.* **2012**, *376*, 322–326. [CrossRef]
59. See, H.; Doi, M. Aggregation kinetics in electro-rheological fluids. *J. Phys. Soc. Jpn.* **1991**, *60*, 2778–2782. [CrossRef]

Disclaimer/Publisher's Note: The statements, opinions and data contained in all publications are solely those of the individual author(s) and contributor(s) and not of MDPI and/or the editor(s). MDPI and/or the editor(s) disclaim responsibility for any injury to people or property resulting from any ideas, methods, instructions or products referred to in the content.